Nanoscale

PAPER

View Article Online
View Journal | View Issue

Cite this: *Nanoscale*, 2017, **9**, 11678

Role of graphene in enhancing the mechanical properties of TiO_2/graphene heterostructures†

Changhong Cao,[a] Sankha Mukherjee,[b] Jian Liu,[c] Biqiong Wang,[c] Maedeh Amirmaleki,[a] Zhuole Lu,[b] Jane Y. Howe,[d] Doug Perovic,[b] Xueliang Sun,[c] Chandra Veer Singh,*[a,b] Yu Sun*[a] and Tobin Filleter*[a]

Received 28th April 2017,
Accepted 24th July 2017

DOI: 10.1039/c7nr03049e

rsc.li/nanoscale

Graphene has been integrated in many heterogeneous structures in order to take advantage of its superior mechanical properties. However, the complex mechanical response of heterogeneous films incorporating graphene is not well understood. Here, we studied the mechanical behavior of atomic layer deposition (ALD) synthesized TiO_2/graphene, as a representative building block of a typical composite, to understand the mechanical behavior of heterostructures using an experiment-computational approach. The inclusion of graphene was found to significantly enhance the Young's modulus of TiO_2/graphene hetero-films for films below a critical thickness of 3 nm, beyond which the Young's modulus approaches that of pure TiO_2 film. A rule-of-mixtures was found to reasonably estimate the modulus of the TiO_2/graphene hetero-film. Experimentally, these hetero-films were observed to fail *via* brittle fracture. Complimentary density functional theory and finite element modeling demonstrates strong adhesion at the graphene TiO_2 interface and that graphene serves as a reinforcement, providing the hetero-film with an ability to sustain significantly high stresses at the point of failure initiation. The results and methodology described herein can contribute to the rational design of strong and reliable ultrathin hetero-films for versatile applications.

Introduction

Heterogeneous thin films are used for a vast array of applications. For example, graphene and boron nitride films are used in photodetectors,[1] graphene and metal oxide films are used for energy storage devices,[2] graphene-hBN–MoS_2 films are utilized in memory devices,[3] and graphene/MoS_2/WSe_2/graphene hybrid films are applied in photovoltaic devices.[4] Atomic layer deposition (ALD) is an effective technique to synthesize conformal and continuous hetero-films,[5,6] by allowing nanoscale control over the thickness of the as-deposited film. The resulting hetero-films are often found to have improved performance as compared to each of the individual constituents. Due to this advantage, hetero-films obtained by ALD deposition of TiO_2 thin films on graphene are widely used in Li^+ and Na^+ batteries,[7–9] supercapacitors,[10] photocatalysts,[11–13] solar applications[14] and sensors.[15,16] Furthermore, as compared to thin films of TiO_2, TiO_2/graphene composites have been demonstrated to impart excellent capacity and cycling stability to energy storage devices,[7] to possess higher photocatalytic degradation efficiency as photocatalysts,[13] and to improve the sensitivity of sensors for material detection.[15,16] Although the use of graphene in these hetero-films is often motivated by its excellent electronic and mechanical properties,[8,17] direct evidence and quantification of how graphene enhances the mechanical stability and durability of such hetero-films is currently lacking. Understanding the mechanical response of hetero-films can help to reduce detrimental factors in their applications. For example, one of the major applications of metal oxide/graphene-based-hetero-films is in lithium ion batteries where mechanical failure-induced electrochemical deterioration is critical.[7] It has been demonstrated that Young's modulus of layered battery materials is closely related to their long-term cycling performance.[18]

Previously, Liu *et al.*[19] characterized the elastic properties of heterogeneous MoS_2/WS_2 films and found that the elastic modulus of the hetero-film is lower than the sum of 2D modulus of each film, due to weak interlayer interactions. Furthermore, Guo *et al.* investigated the theoretical interfacial binding strengths of MoS_2/graphene hetero-films using the

[a]*Department of Mechanical and Industrial Engineering, University of Toronto, 5 King's College Rd, Toronto, ON, Canada, M5S 3G8. E-mail: chandraveer.singh@utoronto.ca, sun@mie.utoronto.ca, filleter@mie.utoronot.ca*
[b]*Department of Materials Science and Engineering, University of Toronto, 184 College St, Toronto, ON, Canada, M5S 3E4*
[c]*Department of Mechanical and Materials Engineering, University of Western Ontario, London, Ontario, Canada N6A 5B9*
[d]*Hitachi High-Technologies Canada, Inc., Toronto, ON, Canada, M9W 6A4*
†Electronic supplementary information (ESI) available. See DOI: 10.1039/c7nr03049e

density functional theory and found strong interfacial binding.[20] Additionally, depending on synthesis conditions, such as the ALD cycle number, the resulting hetero-films can exhibit significantly varying morphology, particle size and growth rate,[21] each of which can significantly alter the mechanical performance of the hetero-film. In general, the number of ALD cycles used for producing the films is often chosen based on the film growth rate and desired film thickness.[2,8,16] However, the effect of the number of ALD cycles on the mechanical characteristics of these heterostructures is not clearly understood. Therefore, a quantitative understanding of how synthesis condition induced structural difference of the deposited film influences on the overall mechanical behavior of the hetero-films is required for material designs with the mechanical durability.

In this work, we studied the mechanical behavior of TiO_2/graphene hetero-films synthesized with a varying number of ALD cycles, and resulting thicknesses. A series of TiO_2/graphene hetero-films were prepared by depositing TiO_2 films on graphene monolayers for a range of ALD cycle numbers (1, 10, 20, 50, 100, 200 and 500 cycles). The resulted hetero-films have TiO_2 films deposited on both sides of the graphene monolayers (Fig. 1) due to the conformal nature of the ALD technique. Monolayer polycrystalline graphene films, suspended over holey silicon nitride transmission electron microscopy (TEM) grids, were transferred into the ALD chamber for the deposition of TiO_2 using titanium isopropoxide and water as precursors at a deposition temperature of 250 °C (growth rate of ~0.025 nm per cycle).[21] Prior to TiO_2 film deposition, Raman spectroscopy measurements[22] were performed to ensure that the graphene films (prepared by Chemical Vapor Deposition) were monolayer in thickness (see ESI, Fig. S1†).

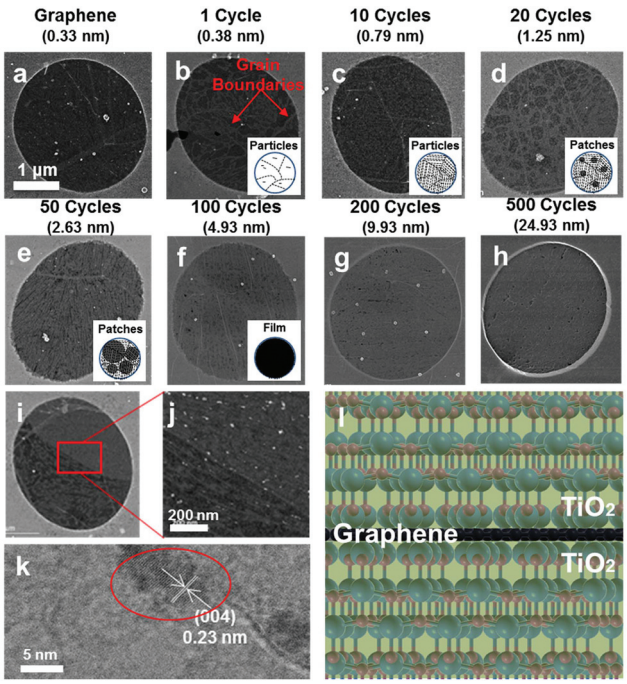

Fig. 1 (a)–(h) STEM images of TiO_2/graphene hetero-films prepared by different numbers of ALD cycles. As ALD cycle number was increased, continuous TiO_2 films gradually formed on both sides of graphene. The inset schematic on each image represents the condition of TiO_2. (i) STEM image of a TiO_2/graphene hetero-film prepared by 20 ALD cycles, undergoing a transition to a continuous layer. (j) Higher magnification snapshot of the region marked in red rectangle in (i). (k) High resolution TEM image of a TiO_2/graphene hetero-film prepared by 100 ALD cycles showing a continuous layer. Red circled region shows the TiO_2 layer exhibiting a lattice spacing of 0.23 nm, corresponding to the (004) plane of anatase TiO_2. (l) Schematic showing the atomic structure of an ideal TiO_2/graphene hetero-film.

Results and discussion

Fig. 1a–h show scanning transmission electron microscopy (STEM) images of TiO_2/graphene hetero-films prepared using different ALD cycle numbers. For hetero-films prepared using 1 & 10 ALD cycles, the TiO_2 films were found to be primarily in particle form due to a discrete number of nucleation sites on the graphene nanosheets.[21] As seen in Fig. 1b, TiO_2 particles were found to be preferably deposited along the graphene defect sites (grain boundaries), which is consistent with previous studies.[23] For 20 & 50 ALD-cycle prepared samples, TiO_2 particles agglomerate into TiO_2 film patches and a film forming transition was revealed (Fig. 1i & j). Thicker hetero-films prepared by 100 ALD cycles and more showed a continuous TiO_2 layer formed on graphene. TEM energy-dispersive X-ray spectroscopy (EDS) elemental mapping on TiO_2/graphene hetero-films further confirmed this gradual evolution of the TiO_2 film formation process with increasing ALD cycles (see ESI, Fig. S2†). Using high resolution TEM, lattice fringes can be seen in samples obtained using 100 ALD cycles or more (Fig. 1k), suggesting continuously formed crystalline TiO_2 sheets. The measured lattice spacing of 0.23 nm corresponds to the (004) plane of anatase TiO_2.[24,25]

To further understand the structure of the TiO_2/graphene hetero-film and study in particular the interfacial adhesion at the TiO_2/graphene interface, density functional theory (DFT) calculations were conducted for the TiO_2/graphene interface (details of DFT simulations can be found in the Methods section). In order to emulate the varying ALD deposition conditions, two distinct scenarios of TiO_2/graphene interfaces were simulated: TiO_2 in the vicinity of graphene and far away from graphene. These two situations give rise to adsorptions commonly known as physisorption and chemisorption, respectively. The charge density difference, interfacial formation energies, vertical distance between the TiO_2 film and graphene formation energies for these two cases are reported in Fig. 2. From the charge density difference plots (Fig. 2a and b) it is clearly seen that in case of chemisorption, there is an increased interaction between TiO_2 and graphene by means of C–O charge sharing. On the other hand, limited charge transfer is observed for the physisorption of TiO_2 over graphene. In the case of chemisorption, the binding energy (−0.41 eV per C atom and −2.46 eV per Ti atom) is comparable to the strong binding predicted for hetero-films such as MoS_2/graphene (−0.154 eV per Mo atom).[20] The binding adsorption

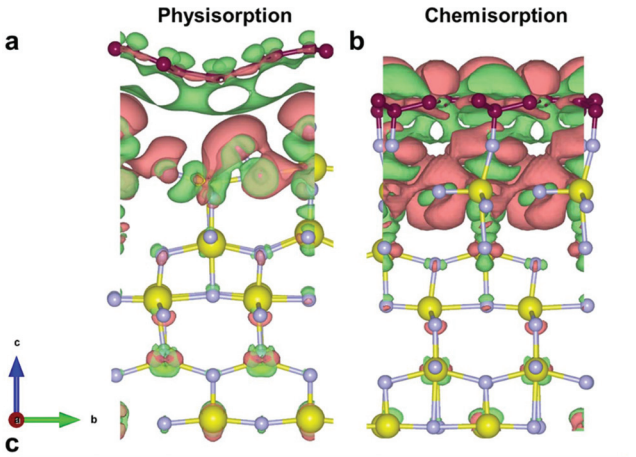

Adsorption type		Chemisorption	Physisorption
Formation energy	per supercell	-9.86 eV	-1.08 eV
	per C atom	-0.41 eV / C atom	-0.04 eV / C atom
	per Ti atom	-2.46 eV / Ti atom	-0.27 eV / Ti atom
Inter-planer distance (Å)		1.41	2.02

Fig. 2 Side views of charge density difference plots for (a) physisorption and (b) chemisorption of TiO_2 over graphene substrate. Color code for atoms: yellow Ti; blue O, brown C. The isosurface level is set to be 0.0004 e $Å^{-3}$. Light red and light green regions indicate charge accumulation and depletion, respectively. (c) The binding energies and interplanar distance for the graphene/TiO_2 heterostructure.

energies of TiO_2 clusters on graphene were also calculated by other studies to be in the range of −1.09 eV to −1.57 eV per cluster,[26] which are in agreement with our current study. Lattice mismatch between the two surfaces leads to compression on graphene and stretching on TiO_2 in the zigzag direction, and negligible changes in the armchair direction. In the case of physisorption, the TiO_2 substrate underwent surface reconstruction and the graphene layer became corrugated. Both calculations have demonstrated that strong adhesion exists at the TiO_2/graphene interface.

The mechanical behavior of TiO_2/graphene hetero-films prepared by different numbers of ALD cycles was investigated using atomic force microscopy (AFM) indentation (Fig. 3a) incombination with finite element (FE) simulations to quantify the effect of the number of ALD cycles on the elastic moduli and to evaluate the influence of graphene on the strength of the hetero-films. Tapping mode AFM topography imaging was performed before and after elastic indentation to ensure that the tested hetero-films contained no major defects prior to indentation and that no significant damage was introduced during the ALD process. For initial elastic indentation testing, the hetero-films were indented to a maximum normal force between 60–130 nN (depending on film thickness) at a constant displacement rate of 10 μm s^{-1}. In all elastic loading tests, no significant hysteresis was observed when comparing the loading and unloading curves (see ESI, Fig. S3†), indicating that the hetero-films experienced pure elastic deformation and no significant slippage occurred either between graphene and TiO_2 or between graphene and the substrate. AFM imaging before and after elastic indentation also revealed no significant change in the surface structure of the tested films. At least five independent indentations were performed on different suspended regions of each TiO_2/graphene hetero-film. Fig. 3b shows the experimental normal force *versus* indentation depth of hetero-films prepared with different ALD cycle numbers. The corresponding FE simulation results are shown with circular symbols. In the FE simulations, a perfect bonding between TiO_2 and graphene was assumed. Good agreement was found between the experimental data and FE simulations, which confirms that there was strong adhesion between graphene and TiO_2 in the experiments also consistent with the earlier DFT predictions. More importantly, from Fig. 3b, it is clearly evident that as the ALD cycle number was increased, higher forces were required for the AFM probe to deflect the hetero-films to equivalent depths, suggesting an increase in mechanical stiffness of hetero-films prepared with a higher number of ALD cycles. In addition, the force–depth curves were found to

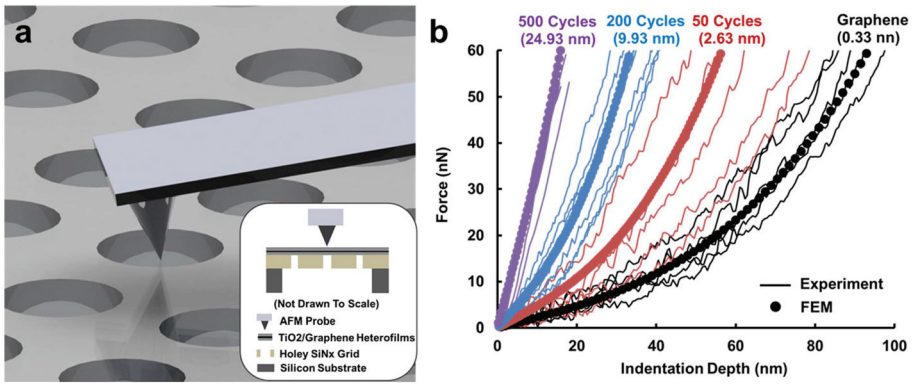

Fig. 3 (a) Schematic of AFM nanoindentation experiment conducted on TiO_2/graphene hetero-films. Films were suspended over holey silicon nitride TEM grids. (Inset) Cross-sectional view. (b) Representative data (force–displacement) from experiments and FE simulations for hetero-films of varying ALD cycles (thickness of the entire film is shown in brackets). Each line represents the loading curve of individual indentations. All hetero-films were indented to the maximum force between 60–130 nN at which no obvious hysteresis was observed, indicating negligible slippage between interfaces.

become more linear as the number of ALD cycles was increased, which implies a more plate-like behavior of the thicker hetero-films during indentation. A highly linear behavior in the elastic regime was observed for the hetero-film prepared by 500 ALD-cycles. This transition in the force–displacement curves indicates a transition from a stretching-dominated (shell) to a bending-dominated (plate) deformation and is consistent with the morphological observations that the formation of TiO_2 on graphene transits from discontinuous particles to continuous films. Bending rigidity can be ignored for shell structures, such as graphene[27] and graphene oxide,[28] but not for plates. Taking bending rigidity into account, the force–displacement behavior of a suspended clamped circular sheet made of a linear isotropic elastic material, under point load in the center of the hetero-film, can be written as eqn (1),[29] which was also used to calculate the Young's moduli of other thin films, such as multilayer MoS_2,[30]

$$F = \left[\frac{4\pi E}{3(1-\nu^2)}\left(\frac{t^3}{a^2}\right)\right]\delta + (\pi T)\delta + \left(\frac{q^3 E t}{a^2}\right)\delta^3 \quad (1)$$

where t is the thickness of the hetero-film, E is the effective Young's modulus of the hetero-film, ν is the effective Poisson's ratio, a is the radius of the suspended hetero-film, T is the pre-tension in the hetero-film, q is a dimensionless parameter, which equals to $1/(1.05 - 0.15\nu - 0.16\nu^2)$, F is the applied force, and δ is the indentation depth. The TiO_2/graphene hetero-films were assumed to be isotropic and elastic, because the hetero-films have a very small thickness to film radius ratio[29,30] (less than 0.1%) such that any shearing effect between the two interfaces can be neglected. For membrane-like structures (pure graphene), only the last two terms in eqn (1) are needed and used for analysis since the bending rigidity for membranes is negligible.[31] For TiO_2/graphene hetero-films, however, the force–depth plots were fit considering the general form [with all three terms in eqn (1)], since there is no clear conceptual distinguishing point to judge whether the hetero-films should be treated as shells or plates.

Fig. 4 presents the experimentally measured Young's moduli of the TiO_2/graphene hetero-films normalized by the measured Young's modulus of graphene as a function of hetero-film thicknesses (estimated based on the ALD growth rate and the number of ALD cycles[21]). The normalized Young's modulus of the hetero-film decreases as the number of ALD cycle increases (Fig. 4). These results demonstrate that before a fully continuous TiO_2 film is formed on graphene (1, 10, 20 and 50 ALD-cycle-prepared), the modulus reinforcement to the hetero-films provided by graphene is present; however, it will diminish as TiO_2 becomes increasingly film-like. It should also be noted that in this thickness regime the experiments exhibit a much higher scatter which is likely due to variations in the film structure in this growth transition regime of the films from particle-like to film-like. When fully continuous films form on graphene (≥100 ALD cycles), the normalized modulus of the hetero-film was found to reach a plateau, indicating that the thickness of the hetero-film gradually has

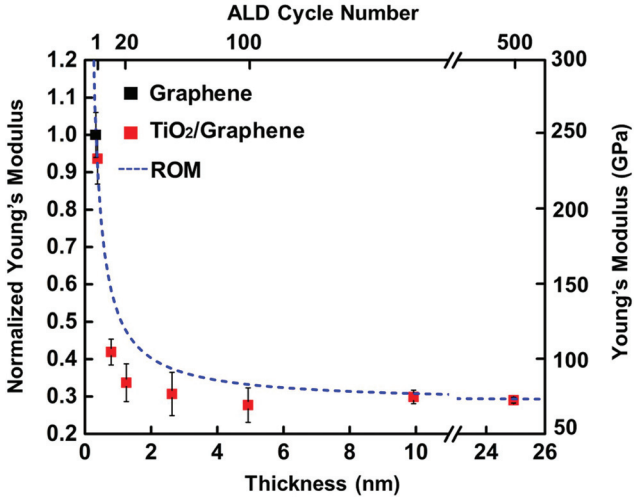

Fig. 4 Normalized Young's modulus *versus* thickness of graphene/TiO_2 hetero-films. For discontinuous TiO_2 layers formed on graphene, the modulus enhancement to the hetero-films provided by graphene gradually becomes insignificant as TiO_2 became more film-like and continuous (1, 10, 20 and 50 ALD cycles). When continuous films formed on graphene (≥100 ALD cycles), the modulus of the hetero-films approached to a constant. The measured normalized moduli of TiO_2/graphene hetero-films are in reasonable agreement with ROM estimates.

minimal effect to its modulus. As the volume ratio of graphene in the thick TiO_2/graphene films is only ~1%, the modulus of the thick TiO_2/graphene films (measured to be 79 ± 18 GPa) is assumed to be close to the modulus of pure TiO_2 film (625 nm, 103 ± 30 GPa).[32] Initially, for ALD cycles lower than 100, graphene acts as the primary load bearing component. However, for films deposited with a higher number of ALD cycles (≥100), the total load is increasingly transferred to the less stiff TiO_2 films.

Utilizing the experimentally measured moduli of graphene, assuming that the modulus of the TiO_2 present is equal to the measured value for plate-like TiO_2/graphene films, and considering the relative volume ratio of each hetero-film, we have calculated the normalized moduli of the hetero-films based on a rule-of-mixtures (ROM)[33] analysis (dashed line in Fig. 4). The low experimentally measured Young's modulus of graphene (~250 GPa) is likely due to ripples[34,35] and residue polymer introduced during its transferring process, which could lower the in-plane stiffness of graphene. As the same graphene samples were used for the entire study, and comparative analysis is the focus of this work, the absolute measured value for the graphene is not believed to significantly affect the trend and findings. It can be seen that the estimated values of the normalized moduli predicted using ROM are in reasonable agreement with the experimental measurements, in particular when TiO_2 was still in the particle form (1 ALD cycle) and when a fully continuous TiO_2 film was formed (≥100 ALD cycles). In the transition regime where TiO_2 forms in patches (20 & 50 cycles), the experimental measurements are found to be lower than those predicted by ROM, possibly due to the fact

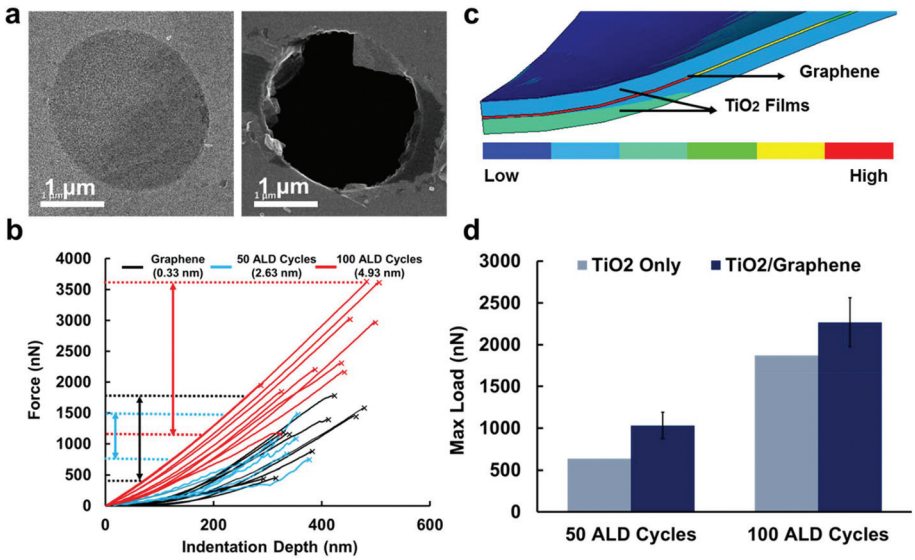

Fig. 5 (a) STEM images of TiO_2/graphene hetero-films prepared by 100 ALD cycles: before and after indentation. (b) Force–displacement plots of indentations for all three cases (thickness of the entire film is shown in brackets). Crosses indicate points of failure. (c) von-Mises stress contour of the hetero-film (100 ALD cycles) at maximum load from FE simulations. (d) Bar graph showing that at maximum stresses, the average maximum loads TiO_2/graphene can withstand from experiment and the maximum load pure TiO_2 films can withstand without graphene estimated from FE simulation, for films prepared with 50 and 100 ALD cycles, respectively.

that although the volume of the TiO_2 films in these cases are relatively large, their microstructure is in the form of either disconnected patches or a non-continuous film. This non-continuous structure of internal islands and disconnected regions of TiO_2 on the graphene sheets would lead to the applied load not effectively being transferred, thus resulting in a lower stiffness of the heterostructure as compared to the ROM predictions.

We next investigated the fracture behavior and effect of graphene to the strength of TiO_2/graphene hetero-films (50 and 100 ALD cycles) by indenting the films to failure. Fig. 5a shows STEM images of hetero-films prepared with 100 ALD cycles before and after indentation to failure. A sudden rupture was observed for both graphene and graphene/TiO_2 structures, which indicates primarily brittle-like failure.[36] The force–indentation depth plots (Fig. 5b) show that all the tested cases exhibit no apparent slippage (which would be indicated by a sudden force drop in the curve), further suggesting that the adhesion between TiO_2/graphene and graphene/substrate interfaces was strong. Five or more different suspended regions were indented for each film thickness reported. The average breaking loads of graphene, 50-ALD-cycle and 100-ALD-cycle prepared hetero-films are 1090 ± 151 nN, 1032 ± 158 nN and 2269 ± 294 nN, respectively. Fig. 5b presents all force–displacement plots from indentations. Crosses indicate points of failure. The close agreement in the force–displacement relationships obtained from experiments and FE simulations (Fig. 3b) permits analysis of stress distribution in the hetero-films at experimentally measured breaking loads in the FE analysis. This continuum-based approach has been previously used for the assessment of stress in monolayer graphene,[31] polycrystalline graphene[27] and graphene oxide membranes.[28] The FE results show that the TiO_2 film at the bottom of the TiO_2/graphene hetero-films experiences larger stresses compared to the layer in contact with the indenter, which is due to larger stretching experienced by the bottom layer (Fig. 5c). This indicates that in the hetero-films, failure is likely initiating from within the bottom TiO_2 layer. Additionally, the maximum stress in graphene at the breaking load is significantly larger than that in TiO_2 for both hetero-films (50 and 100 ALD cycles), which is due to higher stiffness of graphene when compared to TiO_2 layers. Using the maximum stresses in TiO_2, the maximum load that the entire material structure withstands without graphene can be predicted by FE simulations assuming the same layer thicknesses. As can be seen in Fig. 5d, at maximum stress, the structure can withstand significantly less load compared to their graphene hetero-structure counterparts. The loads TiO_2/graphene hetero-structures can undertake are ~63% (1032 nN *vs.* 633 nN) and 21% (2269 nN *vs.* 1871 nN) more than the TiO_2 only cases for the 50 and 100 ALD cycles, respectively. This indicates that graphene indeed provides reinforcement to the hetero-films by undertaking a significant amount of load at high stress levels.

Conclusions

Our quantitative mechanical study demonstrates that the inclusion of graphene can enhance the modulus of the TiO_2/graphene hetero-films with thicknesses less than 3 nm, beyond which the modulus of the structure becomes comparable to that of pure TiO_2 film. In future design of TiO_2/gra-

phene hetero-films for specific applications, the modulus of TiO_2/graphene hetero-films can be estimated using a ROM analysis. In addition, complimentary DFT and FEM study confirmed that the adhesion between graphene and TiO_2 is strong and graphene serves as a reinforcement, providing the hetero-film an ability to sustain significantly higher loads at the point of failure initiation.

This study represents a major first step toward rational design of hetero-films taking advantage of quantitative mechanical analysis. While the AFM based deflection testing used here has the limitation of locally probing mechanical properties and direct tensile testing would be needed in future work for characterize the global behavior, the AFM method does provide the first observations and quantification of the intrinsic nature of strength and fracture in these hybrid structures. The results offer guidelines for the design of TiO_2/graphene hetero-films from a mechanistic standpoint. Mechanical properties of the TiO_2/graphene hetero-films are significantly affected by the thickness. A systematic study on the role of other ALD synthetic parameters (such as deposition temperature and precursor residence time) in the mechanical behavior of hetero-films is needed in the future.

Experimental

AFM nanoindentation

Suspended monolayer CVD grown graphene on holey silicon nitride TEM grid with diameter of 2.5 μm was purchased from Ted Pella Inc., AFM indentation was conducted using an Asylum MFP 3D AFM. The cantilever (All-Diamond Probe, Nano Science Instrument) has a spring constant of 25 N m^{-1} calibrated using the Sader's method.[37] The diamond AFM tip radius was measured by SEM to be 111 nm (see ESI, Fig. S4†). No apparent tip radius change was observed before and after AFM experiments. Before measurement, AFM was stabilized over 24 hours for optimum performance. Errors from experiment are reported in standard error. STEM imaging and EDS elemental mapping were performed after AFM indentation measurement using Hitachi HF 3000 with a beam voltage of 100 keV. Savannah 100 (Cambridge Nanotechnology Inc., USA) was used for ALD. Further details of the ALD process can be found in ref. 19.

FE simulation

Finite element simulations using the ANSYS software package were performed to simulate load-indentation response of the TiO_2/graphene hetero-films following the methodology developed by Lee *et al.*[31] The model was defined as a quarter of a circular membrane of 2.5 μm in diameter, and symmetrical boundary condition was applied on the surfaces in the radially outward direction. The thickness of the graphene was set to be 0.33 nm while the thicknesses of the TiO_2 films were taken as 2.3 nm, 4.6 nm, 9.6 nm and 24.6 nm, estimated according to the ALD growth rate. The AFM tip was modeled as a rigid hemisphere made of diamond with a radius of 111 nm. The contact between the AFM tip and the substrates was assumed to be frictionless. Graphene was assumed to be isotropic with a Young's modulus of 250 GPa and a Poisson's ratio[38] equal to 0.17. TiO_2 films were also considered to be isotropic with a Young's modulus of 79 GPa, estimated by fitting the experimental load-indentation data to the membrane stiffening model (Fig. 3b). A Poisson's ratio of 0.27 (ref. 1) was used for TiO_2. Hexahedral mesh with solid 185 element was used to create the FE model, which contained 100k to 225k elements (see ESI, Fig. S5†).

DFT simulation

Density functional theory (DFT) calculations using the plane-wave basis set were conducted to quantify the binding strength at the TiO_2/graphene interface. The Quantum Espresso software package[39] was employed using the Perdew–Burke–Ernzerhof (PBE) exchange–correlation functional and the Vanderbilt ultrasoft pseudopotential. The kinetic-energy cutoff and the charge density cutoff were set to be 40.0 Ry and 160.0 Ry, respectively. A uniform $4 \times 4 \times 1$ k-point grid and the Methfessel–Paxton (MP) smearing method were applied. To capture the characteristics of TiO_2/graphene interface, a slab model was built with one atomic layer of graphene and 15 atomic layers of TiO_2, terminated at the (004) plane (in consistence with experimental observations). To account for lattice mismatch between the two substrates, the supercell's boundaries were allowed to relax in lateral (x and y) directions, while keeping a fixed vacuum distance of at least 20 Å in the direction (z direction) perpendicular to the xy plane. In the initial setup of the relaxation calculations, the zigzag direction of the graphene layer was assumed to align with the [010] direction of the TiO_2 surface, so that a $p(3 \times 2)$ graphene cell, with minor adjustments in the lattice distance, could be stacked on top of a $p(2 \times 2)$ TiO_2 cell to create a common supercell. The total formation energy of the process was calculated according to

$$E_{\text{binding}} = E_{\text{TiO}_2/\text{graphene}} - E_{\text{TiO}_2} - E_{\text{graphene}}$$

where $E_{\text{TiO}_2/\text{graphene}}$ is the relaxed energy of the hetero-film supercell, and E_{TiO_2} and E_{graphene} are the self-consistent energies of isolated TiO_2 and graphene interfaces isolated. More negative binding energies, therefore, represent larger interface strength. The charge density difference was calculated according to

$$\rho_{\text{diff}} = \rho_{\text{TiO}_2/\text{graphene}} - \rho_{\text{TiO}_2} - \rho_{\text{graphene}}$$

where $\rho_{\text{TiO}_2/\text{graphene}}$ is the charge density of the hetero-film supercell, and ρ_{TiO_2} and ρ_{graphene} are the charge densities of TiO_2 and graphene interfaces. The inter-planer distances were measured by taking the difference in the z-coordinates between the lowest C atom and the highest O atom.

Acknowledgements

The authors acknowledge funding by the Natural Sciences and Engineering Research Council of Canada (NSERC) through Discovery Grants to C. V. S., Y. S, and T. F. and a

grant from Ontario Research Funds – Research Excellence to Y. S. T. F. also acknowledges financial support from the Ontario Ministry of Research and Innovation Early Researcher Award Program and the Canada Foundation for Innovation. C. V. S. acknowledges additional financial support from Mitacs and Ontario Ministry of Research and Innovation Early Researcher Award Program. Y. S. and X. S. also acknowledge financial support from the Canada Research Chairs Program. TEM analysis was carried out at Ontario Center for the Characterization of Advanced Materials (OCCAM). Raman Spectroscopy was conducted in Advanced Optical Microscopy Facility (AOMF). The authors thank Matthew Daly and Yangjie Guo (University of Toronto), James Jonkman (AOMF), and Sal Boccia (OCCAM) for technical assistance and discussions.

References

1 L. Borgese, M. Gelfi, E. Bontempi, P. Goudeau, G. Geandier, D. Thiaudière and L. E. Depero, *Surf. Coat. Technol.*, 2012, **206**, 2459.
2 M. Li, X. Li, W. Li, X. Meng, Y. Yu and X. Sun, *Electrochem. Commun.*, 2015, **57**, 43.
3 M. Sup Choi, G.-H. Lee, Y.-J. Yu, D.-Y. Lee, S. Hwan Lee, P. Kim, J. Hone and W. Jong Yoo, *Nat. Commun.*, 2013, **4**, 1624.
4 G.-H. Lee, C.-H. Lee, A. M. van der Zande, M. Han, X. Cui, G. Arefe, C. Nuckolls, T. F. Heinz, J. Hone and P. Kim, *APL Mater.*, 2014, **2**, 092511.
5 J. Liu and X. Sun, *Nanotechnology*, 2015, **26**, 024001.
6 X. Meng, X.-Q. Yang and X. Sun, *Adv. Mater.*, 2012, **24**, 3589.
7 X. Li, X. Meng, J. Liu, D. Geng, Y. Zhang, M. N. Banis, Y. Li, J. Yang, R. Li, X. Sun, M. Cai and M. W. Verbrugge, *Adv. Funct. Mater.*, 2012, **22**, 1647.
8 C. Ban, M. Xie, X. Sun, J. J. Travis, G. Wang, H. Sun, A. C. Dillon, J. Lian and S. M. George, *Nanotechnology*, 2013, **24**, 424002.
9 C. Chen, Y. Wen, X. Hu, X. Ji, M. Yan, L. Mai, P. Hu, B. Shan and Y. Huang, *Nat. Commun.*, 2015, **6**, 6929.
10 X. Sun, M. Xie, G. Wang, H. Sun, A. S. Cavanagh, J. J. Travis, S. M. George and J. Lian, *J. Electrochem. Soc.*, 2012, **159**, A364.
11 S. Anandan, T. Narasinga Rao, M. Sathish, D. Rangappa, I. Honma and M. Miyauchi, *ACS Appl. Mater. Interfaces*, 2012, **5**, 207.
12 H. P. Wu, D. W. He, Y. S. Wang, B. Y. Yang, H. T. Xu, J. F. Li, H. T. Wang, J. G. Wang and M. Fu, *Adv. Mat. Res.*, 2012, **465**, 80.
13 X. Liu, R. Cong, L. Cao, S. Liu and H. Cui, *New J. Chem.*, 2014, **38**, 2362.
14 C. W. Lai, F. W. Low, S. W. Chong, C. Pp Wong, B. M. Siddick, Z. Siti, J. C. Juan and S. B. Abdul Hamid, *Curr. Org. Chem.*, 2015, **19**, 1882.
15 J. Zhang, C. Zhao, P. A. Hu, Y. Q. Fu, Z. Wang, W. Cao, B. Yang and F. Placido, *RSC Adv.*, 2013, **3**, 22185.
16 H. Zhang, S. Shuang, G. Wang, Y. Guo, X. Tong, P. Yang, A. Chen, C. Dong and Y. Qin, *RSC Adv.*, 2015, **5**, 4343.
17 M. Li, X. Li, W. Li, X. Meng, Y. Yu and X. Sun, *Electrochem. Commun.*, 2015, **57**, 43.
18 Z. Honghe, Z. Li, L. Gao, S. Xiangyun and S. B. Vincent, *J. Power Sources*, 2012, **217**, 530.
19 K. Liu, Q. Yan, M. Chen, W. Fan, Y. Sun, J. Suh, D. Fu, S. Lee, J. Zhou, S. Tongay, J. Ji, J. B. Neaton and J. Wu, *Nano Lett.*, 2014, **14**, 5097.
20 M. Guo, Y. Yang, Y. Leng, L. Wang, H. Dong, H. Liu and W. Li, *J. Mater. Chem. C*, 2017, **5**, 4845.
21 X. Meng, D. Geng, J. Liu, R. Li and X. Sun, *Nanotechnology*, 2011, **22**, 165602.
22 A. C. Ferrari, J. C. Meyer, V. Scardaci, C. Casiraghi, M. Lazzeri, F. Mauri, S. Piscanec, D. Jiang, K. S. Novoselov, S. Roth and A. K. Geim, *Phys. Rev. Lett.*, 2006, **97**(18), 187401.
23 K. Kim, H.-B.-R. Lee, R. W. Johnson, J. T. Tanskanen, N. Liu, M.-G. Kim, C. Pang, C. Ahn, S. F. Bent and Z. Bao, *Nat. Commun.*, 2014, **5**, 4781.
24 W.-J. Ong, M. M. Gui, S.-P. Chai and A. R. Mohamed, *RSC Adv.*, 2013, **3**, 4505.
25 M. Liu, L. Piao, L. Zhao, S. Ju, Z. Yan, T. He, C. Zhou and W. Wang, *Chem. Commun.*, 2010, **46**, 1664.
26 B. Bukowski and N. A. Deskins, *Phys. Chem. Chem. Phys.*, 2015, **17**, 29734.
27 G.-H. Lee, R. C. Cooper, S. J. An, S. Lee, A. van der Zande, N. Petrone, A. G. Hammerberg, C. Lee, B. Crawford, W. Oliver, J. W. Kysar and J. Hone, *Science*, 2013, **340**, 1073.
28 C. Cao, M. Daly, C. V. Singh, Y. Sun and T. Filleter, *Carbon*, 2015, **81**, 497.
29 S. Timoshenko, *Theory of Plates and Shells*, McGraw-Hill, London 1940.
30 A. Castellanos-Gomez, M. Poot, G. A. Steele, H. S. J. van der Zant, N. Agrait and G. Rubio-Bollinger, *Adv. Mater.*, 2012, **24**, 772.
31 C. Lee, X. D. Wei, J. W. Kysar and J. Hone, *Science*, 2008, **321**, 385.
32 P. Soares, A. Mikowski, C. M. Lepienski, E. Santos Jr., G. A. Soares, V. Swinka Filho and N. K. Kuromoto, *J. Biomed. Mater. Res., Part B*, 2008, **84**, 524.
33 M. Alger, *Polymer science dictionary*, Springer Science & Business Media, 1996.
34 C. S. Ruiz-Vargas, H. L. L. Zhuang, P. Y. Huang, A. M. van der Zande, S. Garg, P. L. McEuen, D. A. Muller, R. G. Hennig and J. Park, *Nano Lett.*, 2011, **11**, 2259.
35 R. J. T. Nicholl, H. J. Conley, N. V. Lavrik, I. Vlassiouk, Y. S. Puzyrev, V. P. Sreenivas, S. T. Pantelides and K. I. Bolotin, *Nat. Commun.*, 2015, **6**, 8789.
36 X. Wei, L. Mao, R. A. Soler-Crespo, J. T. Paci, J. Huang, S. T. Nguyen and H. D. Espinosa, *Nat. Commun.*, 2015, **6**, 8029.
37 J. E. Sader, J. W. M. Chon and P. Mulvaney, *Rev. Sci. Instrum.*, 1999, **70**, 3967.
38 M. Kim, C. Lee and J. Jang, *Adv. Funct. Mater.*, 2014, **24**, 2489.
39 P. Giannozzi, S. Baroni, N. Bonini, M. Calandra, R. Car, C. Cavazzoni, D. Ceresoli, G. L. Chiarotti, M. Cococcioni and I. Dabo, *J. Phys.: Condens. Matter*, 2009, **21**, 395502.

